

Coordinated Space- and Ground-based Monitoring of Accretion Bursts in a Protoplanetary Disk: The Orbital and Accretion Properties of DQ Tau[★]

Hala Alqubelat¹, Carlo F. Manara¹, Justyn Campbell-White¹, Monika G. Petr-Gotzens¹, Benjamin M. Tofflemire^{2,3}, Andrea Banzatti⁴, Enrico Ragusa^{5,6}, Emma T. Whelan^{6,7}, Guillaume Bourdarot⁸, Catherine Dougados⁹, Eleonora Fiorellino^{10,11}, Sean I. Mills⁷

¹ European Southern Observatory, Karl-Schwarzschild-Strasse 2, 85748 Garching bei München, Germany

² SETI Institute, Mountain View, CA 94043, USA/NASA Ames Research Center, Moffett Field, CA 94035, USA

³ Department of Astronomy, The University of Texas at Austin, Austin, TX 78712, USA

⁴ Department of Physics, Texas State University, 749 North Comanche Street, San Marcos, TX 78666, USA

⁵ Dipartimento di Fisica, Università degli Studi di Milano, Via Celoria 16, 20133 Milano MI, Italy

⁶ Dipartimento di Matematica, Università degli Studi di Milano, Via Saldini 50, 20133, Milano, Italy

⁷ Department of Physics, Maynooth University, Maynooth, Co. Kildare, Ireland

⁸ Max-Planck-Institut für extraterrestrische Physik, Giessenbachstrasse 1, D-85748 Garching, Germany

⁹ Univ. Grenoble Alpes, CNRS, IPAG, 38000 Grenoble, France

¹⁰ Alma Mater Studiorum – Università di Bologna, Dipartimento di Fisica e Astronomia “Augusto Righi”, Via Gobetti 93/2, I-40129, Bologna, Italy

¹¹ INAF – Osservatorio Astronomico di Trieste, via Tiepolo 11, I-34143 Trieste, Italy

Received September 2025; accepted November 2025

ABSTRACT

Multiplicity in pre-main-sequence (PMS) systems shapes circumstellar and circumbinary disks, often resulting in morphological features such as inner cavities, spiral arms, and gas streamers that facilitate mass transfer between the disk and stars. Consequently, accretion in eccentric close binaries is highly variable and synchronized with their orbits, producing distinct bursts near periastron passages. In this study, we examine the orbital and accretion properties of the eccentric Classical T-Tauri binary star DQ Tau using medium- to high-resolution spectroscopy obtained using the Very Large Telescope (VLT) X-Shooter and UVES instruments. The data have been taken at the time of a monitoring of the inner disk chemistry with JWST, and the results of our analysis are needed for a correct interpretation of the JWST data. We refine the orbital parameters of the system and report an increment in the argument of periastron of $\sim 30^\circ$. This apsidal motion can be caused by the massive disk acting as a third body in the system. We also explore the possibility that the resulting apsidal motion is caused by a still not-detected additional (sub-)stellar companion. In this case, we estimate a lower limit of $\sim 15M_J$ for the mass of this putative companion at the cavity edge ($a = 3a_{\text{bin}}$). We investigate the accretion of the primary and secondary stars in the system using the Ca II 849.8 nm emission line. We observe the primary accretes more at the periastron compared to its previous quiescent phases. The secondary dominates the accretion at post-periastron phases. Additionally, we report an elevated L_{acc} at apastron, possibly due to the interaction of the stars with irregularly shaped structures near their closest approach to the circumbinary disk. Finally, we derive the accretion luminosity of each star across the disentangled epochs and compare the results to those derived by the UV excess, finding a good overall agreement. The individual L_{acc} values can be used as an input for the chemical models.

Key words. stars: DQ Tau – stars: pre-main sequence – stars: variables: T Tauri – accretion – binaries: spectroscopic

1. Introduction

High-angular-resolution observations and theoretical models of young stellar objects (YSOs) have highlighted the impact of multiplicity on the surrounding disk, often manifesting as prominent morphological features such as inner cavities, spiral arms, streamers, and more (e.g., Benisty et al. 2023). Numerous theoretical work put these features in relation to the presence of stellar or planetary companions (Bae et al. 2023).

Both GG Tau and HD 142527 show strong tidal interactions between their stellar companions and surrounding disks, produc-

ing gas flows from circumbinary to circumstellar regions. In both systems, these interactions shape disk structures, including inner cavities, asymmetries, and spiral arms, highlighting the role of companions in driving ongoing disk dynamics (Keppler et al. 2020; Toci et al. 2024; Verhoeff et al. 2011; Biller et al. 2012; Nowak et al. 2024).

Similarly, AK Sco, with a separation of ~ 0.16 au, exhibits periodic enhancements in X-ray and UV emissions, attributed to accretion streams crossing the inner cavity and delivering material onto the stellar surfaces (Gómez de Castro et al. 2013). Complementary studies of CoKu Tau/4 revealed an inner cavity carved by the binary’s gravitational influence (Ireland & Kraus 2008).

[★] Based on observations collected at the European Organization for Astronomical Research in the Southern Hemisphere under ESO programs 114.2799.001, 114.27MG.001, and 082.C-0218(A).

Pre-Main-Sequence (PMS) accretion is a stochastic process giving rise to variability on timescales from hours to decades (Hartmann et al. 2016). PMS stars can witness routine-like variability with 1-2 mag change in brightness for up to weeks, while burst-like variability does increase brightness 1-2.5 mag, from a week up to a year (Fischer et al. 2023). Meanwhile, the presence of binary companions is expected to produce accretion variability with characteristic frequencies corresponding to their orbital timescales and sub-harmonics, leading to pulsed accretion in eccentric systems (Artymowicz & Lubow 1996; Ragusa et al. 2016; Teyssandier & Lai 2020).

Accretion flows in close binary systems are enhanced by dynamical interactions that periodically channel material from the circumbinary disk onto the individual stars. This process tends to preferentially feed the lower-mass companion, driving the system towards mass ratio unity over time (Tokovinin 2000; Bate 2000), with differences expected depending on disk parameters, binary mass ratio, and orbital eccentricity, and the precession angle between disk and binary stars (Young et al. 2015). This accretion-driven mass equalisation may be the origin of the observed peak in the mass ratio distribution of close binaries around $q \approx 1$.

Muñoz & Lai (2016) performed 2D simulations on accretion flows in the circumbinary cavity of an equal-mass binary. They showed that the circumstellar disks of eccentric binaries are severely truncated at pericenter. The circumstellar disks show differences in their surface densities, implying that the two stars of the equal-mass binary accrete at different rates. This was also shown by Günther & Kley (2002), who demonstrated that accretion in close to equal-mass binaries is highly time-variable and not equally distributed among the two components of the system. This effect is driven by asymmetries in the circumbinary flow at the various phases of the orbital period.

Observational monitoring supports such theoretical models, as accretion variability of young spectroscopic binaries is readily observed. Tofflemire et al. (2017b, 2019) showed that the eccentric TWA 3A ($e = 0.63$, $q = 0.84$) experience periodic accretion bursts near periastron passages, with accretion rates increasing by a factor of ~ 4 . Using the emission line of He I 5876Å, they showed that circumbinary accretion streams preferentially feed the primary star. In the case of the multiple system VW Cha (Zsidi et al. 2022), a peak-to-peak photometric variability amplitude of up to ~ 0.8 mag was observed, which was attributed to changes in the accretion rate, possibly influenced by the multiplicity and the presence of a circumbinary disk. Similarly, the WX Cha binary system exhibits variability with a photometric amplitude up to ~ 0.5 mag Fiorellino et al. (2022b). Another examples is CVSO 104 ($e = 0.4$, $q = 0.9$), where both components exhibit similar levels of accretion, as indicated by He I 6678/5876Å and Balmer emission line profiles, accreting from a shared circumbinary disk (Frasca et al. 2021).

Key questions remain about how binary properties, particularly eccentricity, mass ratio, and orbital phase-modulated accretion dynamics shape the structure of the inner disk. These interactions not only shape disk morphology but are crucial for interpreting time-sensitive spectroscopic observations, especially in systems where both stars are actively accreting, leading to large orbit-to-orbit variability. The impact of variability on the physical and chemical conditions of the inner disk also remains open. The simultaneous accretion monitoring is particularly crucial to be able to interpret the JWST MIR spectra, which are rich in molecular lines, originating from the inner regions of the disk (Banzatti et al. 2023; Grant et al. 2023). Hence, characterising

the overall binary accretion behaviour, ideally disentangling the contribution of each component, driven by the binary configuration is essential for understanding the observable chemistry, and structure of the inner disk, where planet formation takes place (Hyden et al. in prep. Kóspál et al. 2025).

This work focuses on DQ Tau, a double-lined spectroscopic binary where both components are of M0 spectral type. The system is located at RA 04^h 46^m 53^s.058, Dec +17° 00' 00".14, and it has a total mass of $M_{1+2} = 1.21 \pm 0.26 M_{\odot}$ as derived from radial velocity measurements and ALMA CO disk modeling (Czekala et al. 2016). The orbital period of the binary has previously been reported to be ~ 15.8 days (Mathieu et al. 1997; Pouilly et al. 2024) with the orbit highly eccentric ($e \sim 0.6$). This system has become a benchmark for studying pulsed accretion. DQ Tau exhibits recurrent accretion bursts near periastron (Tofflemire et al. 2017a; Bary & Petersen 2014; Fiorellino et al. 2022a; Tofflemire et al. 2025) with both components actively accreting. Using 8 epochs of spectroscopic data obtained with the ESO Very Large Telescope (VLT) X-Shooter instrument, Fiorellino et al. (2022a) showed that the primary and secondary accretes at different phases in the orbit with the dominant accretor alternating between the two star. Recently, Pouilly et al. (2024), used the high-resolution CFHT/ESPaDOnS spectrograph to cover one orbital period of this system. They reported that both stars accrete with the primary accreting more compared to previous orbital cycles, resulting in a balanced accretion between the two stars; While in Pouilly et al. (2023), it was noted that the secondary is the dominant accretor.

The analysis of the VLT/X-Shooter data, to be used also in this work, as well as LCO u' photometry obtained in a joint JWST and ground-based campaign to monitor DQ Tau, revealed that the accretion rate can vary by nearly two orders of magnitude near periastron across ten orbits (Tofflemire et al. 2025). In order to correctly interpret the JWST data, a detailed knowledge of the orbital and accretion proprieties of DQ Tau at the time of JWST monitoring is essential. In this work, we use the ground-based observations (VLT/X-Shooter and VLT/UVES) from this monitoring to refine the orbital parameters of DQ Tau. We then trace the accretion of each star across various orbital cycles to estimate the mass accretion rates of each stellar components, complementing on Tofflemire et al. (2025), who only considered the total accretion rate on the binary.

The paper is structured as follows. A description of the observations is provided in Sect. 2, whereas the results on the orbital and accretion properties are presented in Sect. 3. We then discuss the results of the orbital and accretion properties separately and compare them to the literature in Sect. 4, before concluding this paper in Sect. 5.

2. Observations and data reduction

In Fig. 1, we present an overview of the data sets included in this paper, using the time-series accretion-luminosity measurements for the combined accretion rates measured from Tofflemire et al. (2025). The binary periastron passages, the time where accretion bursts happen like clock-work, are marked as dotted vertical lines.

2.1. VLT/X-Shooter

We observed DQ Tau with the X-Shooter spectrograph (Vernet et al. 2011) mounted on the ESO Very Large Telescope (VLT) during the program 114.2799.001 (PIs: C.F. Manara, B.

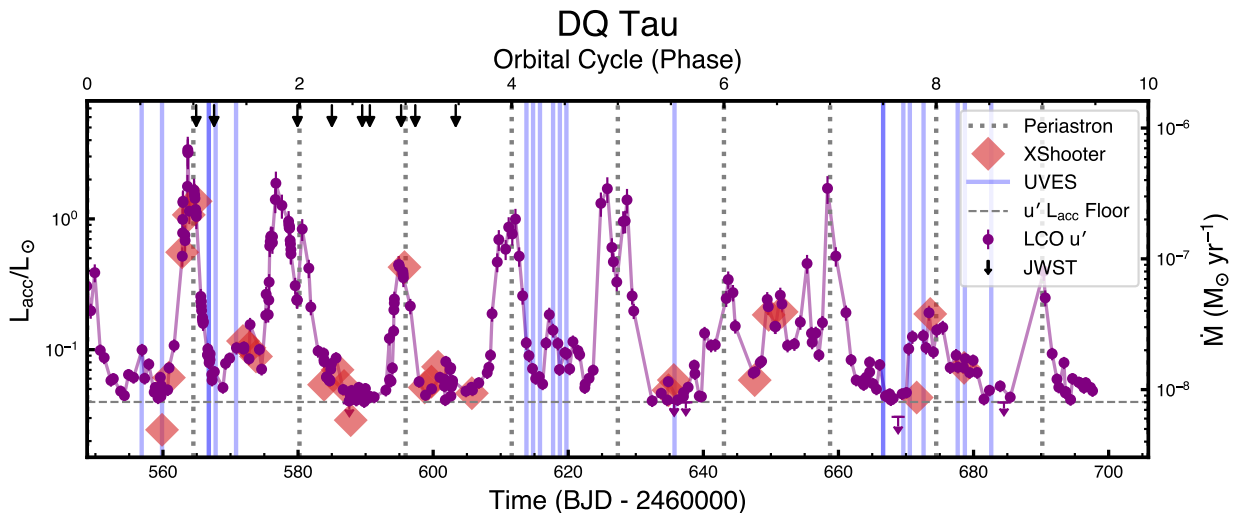


Fig. 1: Accretion variability of DQ Tau shown by observations with LCO u' photometry, X-Shooter, and UVES taken across 5 months between August 13th, 2024 to January 22nd, 2025. The accretion luminosity (left axis) and mass accretion rate (right axis) are measured from X-Shooter spectra and LCO u' -band photometry for the whole system (Tofflemire et al. 2025). Time is reported in barycentric Julian days on the bottom axis and the binary orbital cycles are labelled on the top axis. Vertical dotted lines mark the periastron passages of DQ Tau with the JWST MIR observations indicated as black arrows.

Tofflemire). This spectrograph works at medium resolution ($R \sim 10,000 - 20,000$) and simultaneously covers the wavelength range $\sim 300-2500$ nm, dividing the spectra in three arms (UVB, VIS, NIR). Our observations are set to achieve the highest possible resolution, therefore using the narrowest slits ($0.5'', 0.4'', 0.4''$ in the three arms, respectively), while achieving absolute flux calibration accounting for the slit losses with a short exposure with the broad slits of $5.0''$ width prior to the narrow slit observations. A nodding cycle consisting of four positions ABBA was used for the narrow slit observations to achieve a better sky subtraction at near-infrared wavelengths. The observing strategy was optimized to complement each JWST observation with three X-Shooter spectra.

An absolute time interval was set to start the X-Shooter monitoring in each flare event covered by JWST–MIRI (see Hyden et al. in prep. for JWST observations strategy), and the subsequent epochs were put in relative time-link intervals with minimum distances between the observations of 10 hours. A total of 25 spectra were taken, 19 of them close in time to the JWST observations between September 5th and November 21st, 2024. Not all of the planned spectra were taken on the expected time-interval due to different causes, including interventions on the telescopes and visitor mode runs. As a result, a total of six spectra were observed between December 2nd 2024 and January 3rd, 2025 (see Fig. 1). All data were taken with excellent sky transparency conditions (“clear” or “photometric”).

Data were reduced using the ESO pipeline for X-Shooter v.3.6.8 (Modigliani et al. 2010) in the Reflex environment (Freudling et al. 2013). Telluric lines were removed with the ESO Molecfit tool (Smette et al. 2015), and the final flux calibration was obtained rescaling the narrow slit spectra to the wide slit ones, following the procedure described by Manara et al. (2021). We estimated the S/N in four nm wavelength window for the visual arm at $\lambda = 786$ nm for each epoch. The VIS arm has the highest precision and accuracy of wavelength calibration with a standard deviation of ~ 0.5 km s $^{-1}$. We report the observations log and estimated S/N at wavelength range between $\lambda = 784$ nm and $\lambda = 788$ nm in Table D.1.

2.2. VLT/UVES

During the same monitoring program, DQ Tau was observed also with the UVES spectrograph (Dekker et al. 2000) mounted on the VLT during the program 114.27MG.001 (PI: E. T. Wheelan). The motivation for this programme was to use spectro-astrometry to study changes in the spatial properties of the [O I] 6300 emission from DQ Tau (Mills et al. in prep). We used the RED setting centered at 580 nm, with slit width of $0.8''$, giving a resolution $R \sim 50,000$ and covering the wavelength range $\sim 480-680$ nm. Data were taken between September 2nd, 2024 and January 8th, 2025, always with excellent sky transparency conditions (“clear” or photometric”). A total of 20 epochs were taken (see Fig. 1).

Data were reduced using the ESO pipeline for UVES v.6.4.10 (Ballester et al. 2000) in the Reflex environment (Freudling et al. 2013). The data delivered by the pipeline were flux calibrated, although not corrected for slit losses. Data were not telluric corrected. Instead, we avoided regions where telluric lines are strong in the UVES spectrum in the analysis. For each epoch, we estimated the S/N in four nm wavelength wide region for the red arm at $\lambda = 6654$ Å. We report the observations log and the corresponding S/N at wavelength range between $\lambda = 6652$ Å and $\lambda = 6656$ Å in Table D.1.

We also obtained from the ESO archive the data for a template star, Tyc7760283-1, obtained under program ID 082.C-0218(A) (PI: C. H. F. Melo). We reduced the spectrum using the same version of the ESO pipeline for UVES v.6.4.10 in the Reflex environment as for the DQ Tau spectra.

3. Analysis

In this section, we present the results obtained from the datasets described in Sect.2. We fit the radial velocity (RV) measured on absorption lines to determine the orbital parameters of DQ Tau. Then, we use the Ca II 849.8 nm emission line and Li 670.8 nm absorption line to trace the effect of accretion on line emission and veiling for each component of DQ Tau.

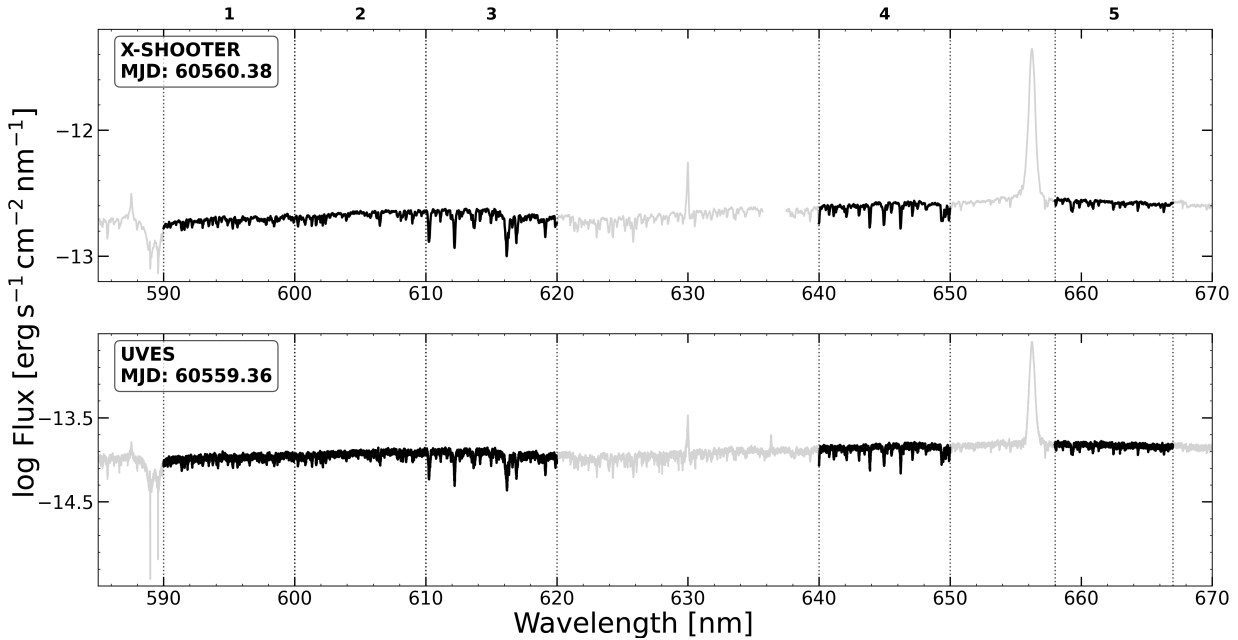


Fig. 2: Spectra of DQ Tau taken with the visual arm of X-Shooter and with UVES. The wavelength ranges in black (590–600, 600–610, 610–620, 640–650, 658–667 nm) correspond to the five regions where the broadening function was calculated for each epoch. The wavelength ranges were chosen to be free of strong emission lines and telluric contamination.

3.1. Orbital properties from the RV analysis

In Fig. 2, we show examples of X-Shooter and UVES spectra of DQ Tau, covering the wavelength ranges used for the analysis. We select five wavelength ranges in common between X-Shooter and UVES to calculate the RV, each of them ten nm wide. The visual arm spectrum of X-Shooter (450–1000 nm) gives the highest resolution approximately $R \sim 20000$, compared to the UVB and NIR arm, and it is therefore the best suited for this study. For UVES, we use the wavelength range 5800–6800 Å, which overlaps with the coverage of X-Shooter, as the rest of the spectrum is affected by the presence of emission lines or strong telluric features. In addition, the bluer parts of the UVES spectrum exhibits lower S/N.

We use a total of 45 spectra to carry out the radial velocity measurements. Each spectrum is corrected to the barycentric velocity frame using `pyasl.baryCorr`¹. We then compute the broadening function (BF), implemented in SAPHIRES², for each spectrum using a class III M0 spectral type template star (TYC7760283-1) with a $v \sin i$ of 14.4 ± 0.5 km s⁻¹ (Stelzer et al. 2013). We note that this value of $v \sin i$ is in the order of the vsini of DQ Tau (Czekala et al. 2016). The X-Shooter spectrum for the template is taken by Manara et al. (2013), while the UVES one is used here for the first time.

The RV of the X-Shooter and UVES templates are obtained using STAR_MELT(Campbell-White et al. 2021)³, calculating a cross-correlation function (CCF) in 100 Å region, free of emission lines, between 5000–6000 Å, with the standard RV template star used in the package.

The final RV of the template is the mean value of all the shifted CCF sections. The RVs of the templates are consistent

between the two spectra $\sim 6.4 \pm 0.1$ km s⁻¹ and 6.6 ± 0.1 km s⁻¹, respectively. The values are in agreement with the RV derived by Fiorellino et al. (2022a).

The produced BF for each DQ Tau spectrum spans an interval of -100 km s⁻¹ to $+100$ km s⁻¹. Double-peaked BFs with clearly separated or blended peaks are fitted with two Gaussian profiles in SAPHIRES. Single narrow-width peaks are fitted with a single Gaussian profile.

The peaks of the BF are considered to be the RV of each component at the time of the observation. The derived RV values are then assigned to the primary and secondary stars based on the fitted amplitudes of each RV curve. By calculating RVs across several wavelength regions, we confirm that the RVs are consistent with each other across the whole range of wavelengths of the spectra for each epoch. Based on this, we calculate the mean RV across the wavelength ranges and the standard deviation for each epoch (Fig. A.2). The extracted mean RV values and errors for each epoch are reported in Table D.1.

We use a Lomb-Scargle Periodogram to look for the binary orbital period signal on the measured RVs. The periodogram yields a detection at period of 15.698 ± 0.105 days when the RVs of the primary or of the secondary are used. A one percent false alarm probability (FAP) threshold is also computed to determine the power level above which signals are considered statistically significant, finding that only this peak is statistically sound (Fig. 3). To estimate the uncertainty in the detected periodic signal, we employ a bootstrapping approach, generating 200 periodograms by randomly resampling the RV measurements with replacement and calculating the standard deviation of the signal within the 14–16 days range.

Mathieu et al. (1997) and Czekala et al. (2016), report a period at 15.8 days based on photometric data from Berkeley Automated Imaging Telescope with V, R, and I bandpasses, with a baseline observations of 5000 days. Additionally, Pouilly et al. (2024) reports a period of $P = 15.8$ days based on a fit of 11

¹ <https://pyastronomy.readthedocs.io/en/latest/pyaslDoc/aslDoc/baryvel.html>.

² <https://github.com/tofflemire/saphires/tree/master>

³ https://github.com/justyncw/STAR_MELT

spectra taken over 40 nights using the Levenberg–Marquardt algorithm. The values of the period derived from our periodogram analysis is thus consistent with the values reported in the literature. Additionally, we use the Markov Chain Monte Carlo (MCMC) approach, described below, to fit for the orbital period along with the other orbital parameters. The derived period from this fit is $P = 15.71 \pm 0.07$ days, also consistent with the result from the periodogram analysis and the literature. We thus adopt this latter period estimates in the following analysis.

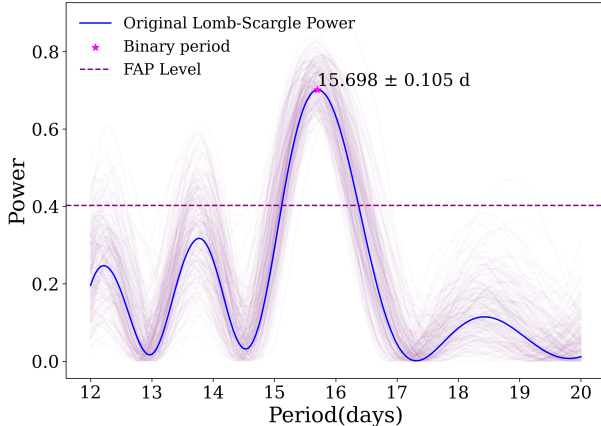


Fig. 3: Lomb-Scargle Periodogram of RV1 data. The data shows a significant peak reported at 15.698 day. The 1% false alarm probability (FAP) level is indicated by the magenta dotted line. In the background, the bootstrapped periodograms are shown in purple.

Table 1: Spectroscopy orbital elements of DQ Tau.

Element	Value
P (days)	15.71 ± 0.07
γ (km s^{-1})	20.33 ± 0.07
K_1 (km s^{-1})	19.03 ± 0.14
K_2 (km s^{-1})	20.10 ± 0.17
e	0.5463 ± 0.0077
ω (degrees)	264.22 ± 0.01
T_0 (MJD)	60564.50 ± 0.02
$q = M_2/M_1$	1.05622 ± 0.0095
$M_1 \sin^3 i$ (M_\odot)	0.0573 ± 0.001
$M_2 \sin^3 i$ (M_\odot)	0.0542 ± 0.001
$a_1 \sin i$ (au)	0.0230 ± 0.0001
$a_2 \sin i$ (au)	0.0243 ± 0.0001
$a \sin i$ (au)	0.04733 ± 0.0002
$a \sin i$ (R_\odot)	10.18 ± 0.04

We fit the RV data using an MCMC approach to determine the orbital parameters of the binary. The model fits the RV curves of a spectroscopic binary system using a Keplerian orbital model. The radial velocities of the two stars, $v_1(t)$ and $v_2(t)$, as functions of time t , derived from the solution to Kepler's equations. First, the mean anomaly is computed:

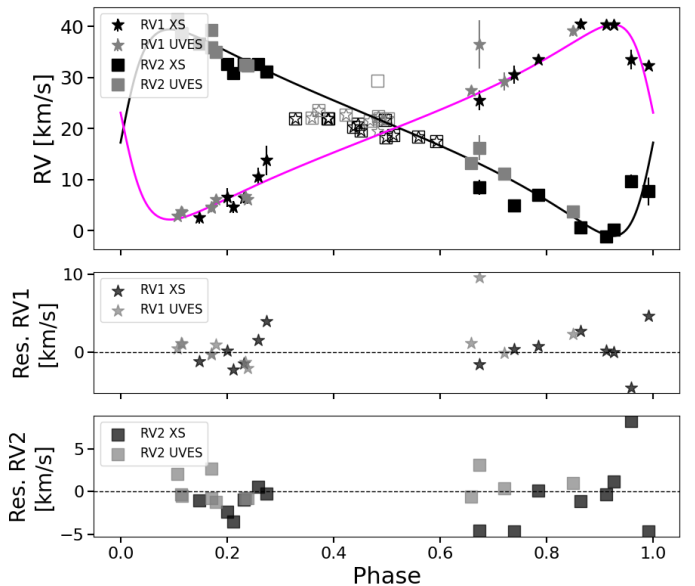


Fig. 4: The orbital solution for DQ Tau in phase. The magenta and black lines fit the primary and secondary data taken with X-Shooter and UVES, respectively. The RVs shown in open symbols at $\sim 0.3 - 0.6$ in phase are discarded from the fitting procedure. Below, the residuals of the fitted model in phase.

$$M(t) = \frac{2\pi(t - T_0)}{P}, \quad (1)$$

where T_0 is the time of periastron passage and P is the orbital period. This is converted into the eccentric anomaly E by numerically solving Kepler's equation:

$$E - e \sin E = M, \quad (2)$$

with e as the eccentricity. The true anomaly θ is then calculated from E , and the RVs are given by:

$$v_1(t) = -K_1 [\cos(\theta + \omega) + e \cos(\omega)] + V_0, \quad (3)$$

$$v_2(t) = K_2 [\cos(\theta + \omega) + e \cos(\omega)] + V_0, \quad (4)$$

where K_1 and K_2 are the velocity semi-amplitudes of the primary and secondary stars, ω is the argument of periastron, and V_0 is the systemic velocity.

The model evaluates the log-likelihood by comparing these predicted RVs to the observed RVs of both stars, using observational uncertainties (the standard deviation of the mean RV), calculated across the different wavelength regions, of each spectrum. We use the emcee⁴ sampler, with 50 walkers and typical runs of 5000 to 10000 steps. An initial burn-in phase of 500 to 1000 steps is discarded. In the fit, we discard the RVs where the BFs from the two stars are blended. The values discarded correspond to epochs at phase (ϕ) $\sim 0.3 - 0.6$, shown as open symbols (Fig. 4). The resulting fit is consistent with the solution when we consider the whole set of data, with the only exception for the eccentricity (e), for which we report a value of $e \sim 0.59$ at $P = 15.698$. We use the parameters corresponding to the maximum likelihood values as best estimates of the model parameters. These are reported in the upper part of Table 1.

⁴ <https://emcee.readthedocs.io/en/stable/>

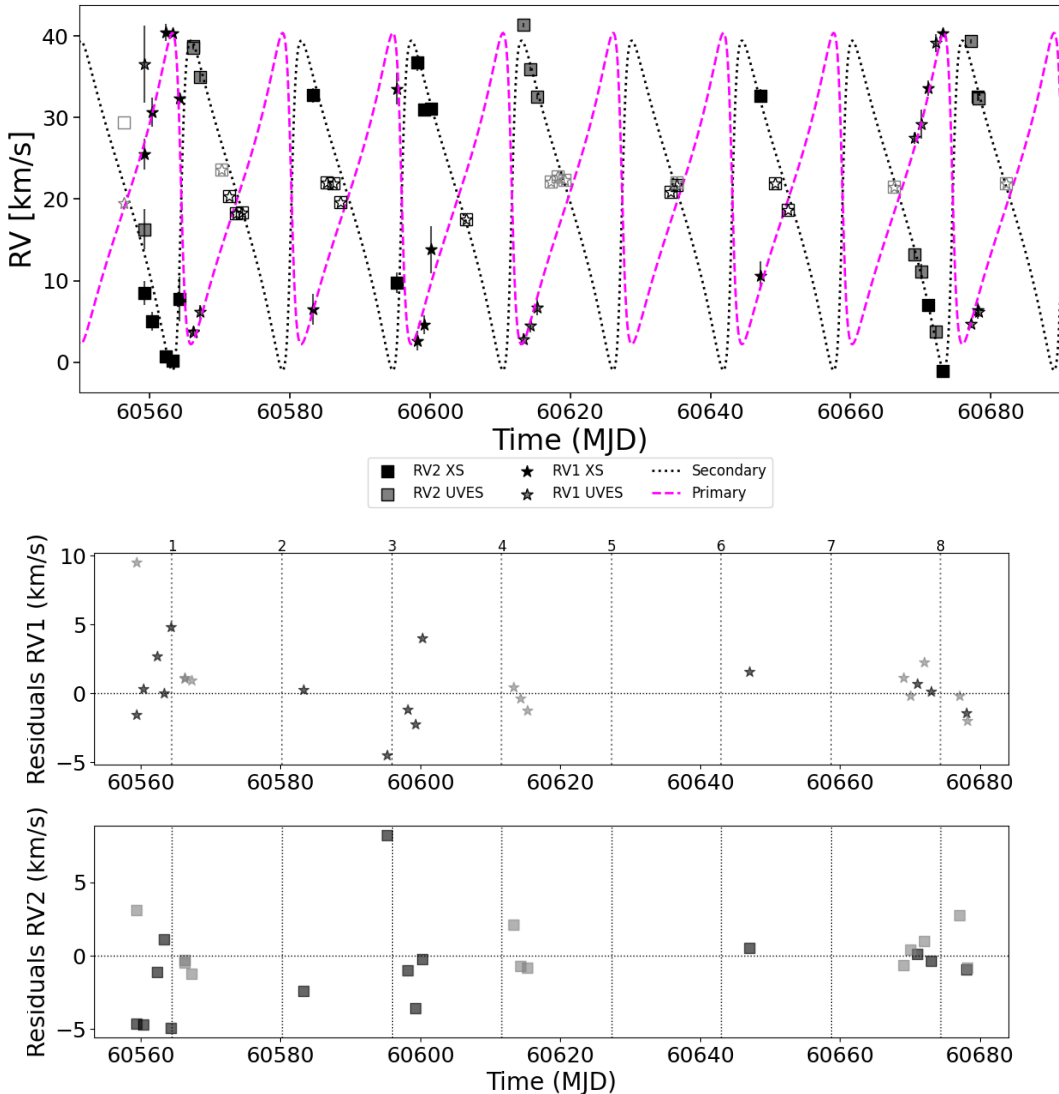


Fig. 5: Orbital solution for DQ Tau across multiple orbits. The magenta and black lines fit the primary and secondary data taken with X-Shooter and UVES, respectively. The RVs shown in open symbols are discarded from the fitting procedure. Below the residual plot. The number of DQ Tau orbital cycles is marked in vertical grey dashed lines.

Fig. 4 shows the phase-folded fit of the RV data with the residuals. The uncertainty on the parameters is taken to be half the difference between the 84th and 16th percentiles, providing an estimate of the 1σ confidence interval. We then calculate the projected masses, separations, and the mass ratio. The corner plot shows the Markov chain resulting from the fit (Fig. A.1).

The MCMC fit is performed leaving the period as a free parameter. On top of that, we also perform a fit using the period obtained from the periodogram, 15.698 days, and one using the period reported in the literature ~ 15.8 days. The orbital solution parameters are consistent in the three cases.

Our data cover a period of more than four months, meaning that we observe almost nine orbits of DQ Tau. In Fig. 5, we show the RVs reported at different orbital cycles. The RV values discarded from the fit are shown as open symbols correspond to where the broadening function becomes single and therefore is challenging to distinguish the contribution of the primary and secondary at the resolution of X-Shooter and UVES.

We investigate the potential influence of the accretion variability of DQ Tau on the measured residuals by examining the

accretion rates derived by Tofflemire et al. (2025), using X-Shooter and LCO u' photometry. The accretion rates corresponding to the UVES epochs are estimated through linear interpolation of the logarithmic accretion rates, $\log_{10} \dot{M}_{\text{acc}}$, to the respective UVES Barycentric Julian Dates (BJDs). Our analysis reveals no significant correlation between the accretion burst activity near periastron and increases in the radial velocity residuals at any epoch.

3.2. Accretion properties from lines

In this section, we aim to study the accretion properties of each component of the DQ Tau binary system across different orbital phases, to determine which star is dominant in accretion across the nine orbital cycles. We first consider the absorption line veiling due to accretion, as measured from the Li 670.8 nm line as we separate this into two distinct components associated to each star. We discuss in Appendix B how this information can be used to trace accretion. Then, we aim to use emission lines to measure the accretion rate. After exploring all the emission lines that trace

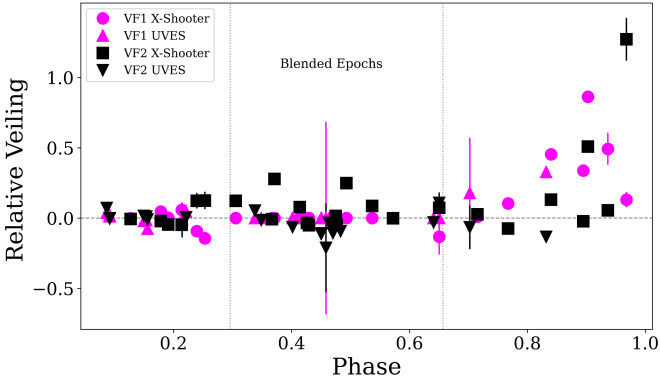


Fig. 6: Relative veiling for primary and secondary using the equivalent width measurements of the Li 670.8 nm line present in X-shooter and UVES datasets. The dashed vertical lines mark the epochs, where originally one EW value was derived from the Gaussian fitting of line. We then de-blend these values as prescribed in Sec.3.2. The relative veiling increases in an order of magnitude as the star approaches periastron.

accretion in the spectra, we notice that most lines are excessively broad or complex (Fig.C.1, Fig.C.3, Fig.C.2), complicating the distinction between the two stellar components contribution, as reported also by Fiorellino et al. (2022a). The best line to be used for the analysis is the bluest of the Ca II triplet lines at 849.8 nm present in the X-Shooter spectra. It has a narrow component and traces the post-shock region close to the stellar surface. The other Ca II triplet lines show consistent profiles. In this paper, we use this line to explore the accretion properties of each star.

3.2.1. Relative veiling measurements

In order to estimate the veiling on each component, we measure the equivalent width (EW) by fitting two Gaussian profiles on the Li 670.8 nm line and deriving the EW as:

$$EW_i = \int \left(1 - \frac{F_{\lambda,i}}{F_c}\right) d\lambda, \quad (5)$$

with $F_{\lambda,i}$ being the best fit profile of each component, labelled with i , and F_c the continuum flux. For the fit, we use the information on the estimated RVs of each epoch from Sec. 3 as an initial guess for the absorption peak velocity of each Gaussian component. As shown in Campbell-White et al. (2023), we assume that one Gaussian absorption component is sufficient to model the entire contribution of each star to the Lithium absorption line.

We then estimate the relative veiling for each star in the binary system and at each epoch as

$$VF_i = \overline{EW_{1,2}}/EW_i - 1, \quad (6)$$

where $\overline{EW_{1,2}}$ corresponds to the mean equivalent width for the primary and secondary among the values measured at $\phi < 0.2$. In this analysis, both the X-Shooter and UVES data are used together. At phases $0.3 < \phi < 0.6$ when the two components of the Lithium line from the two stars are fully blended, only one EW value is measured from the data, corresponding to the blend of the two components. We infer the EW_2 of these epochs by subtracting the mean of EW_1 of the earlier epochs at $\phi < 0.2$. We then assume the EW_1 of these epochs as the mean value.

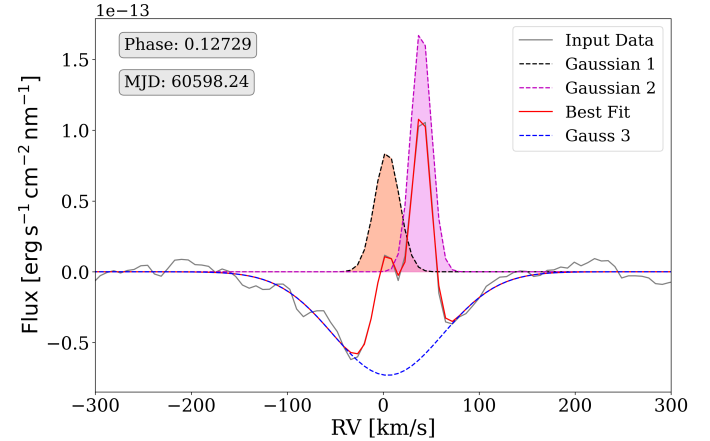
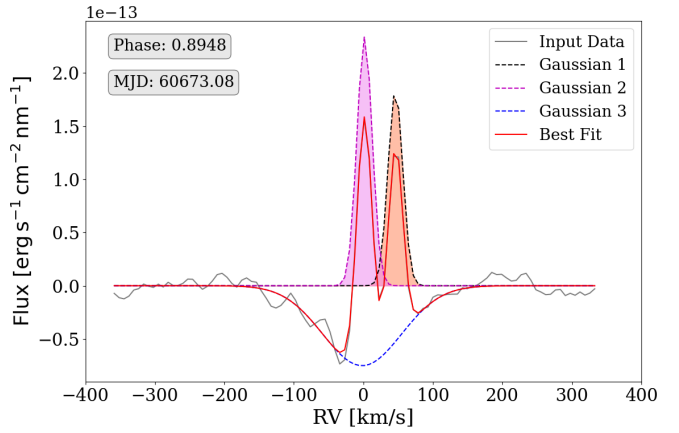


Fig. 7: X-Shooter/Ca II 849.8 nm line at periastron in the last orbital cycle. The double-line feature in grey is fitted using three Gaussian profiles in black, magenta, and blue. The third component in blue is used to subtract the absorption features around each peak in emission. Shaded regions represent the integrated flux of each component. Bottom, X-Shooter/Ca II 849.8 nm in the post-periastron phase of the middle orbital cycles. The double-line feature in grey is fitted using two Gaussian profiles in black and magenta. Shaded regions represent the integrated flux of each component.

We estimate the errors on the EW measurements by generating 50 bootstrapped EW values for each epoch. We introduce random perturbations in the initial guess of the centroid of each Gaussian fitted to the Li 670.8 nm line from a normal distribution with a standard deviation of 1 km/s. The standard deviation of the measured EW in this bootstrapping is then assumed to be the uncertainty on the EW values. The uncertainty on the epochs where the two lines are blended are assumed to be twice the initial error on the blended EW value. We then propagate these uncertainties to the relative veiling measurement.

In Fig. 6, we show the relative veiling estimated for each epoch across the phase. The relative veiling increases as the star approaches periastron $0.7 < \phi < 1.0$, and reaches more than unit value as the accretion bursts arise (Fig. 1). The measured relative veiling of the primary (VF_1) shows how the accretion drastically increases by ~ 1 dex at periastron compared to its previous quiescent state at preceding phases.

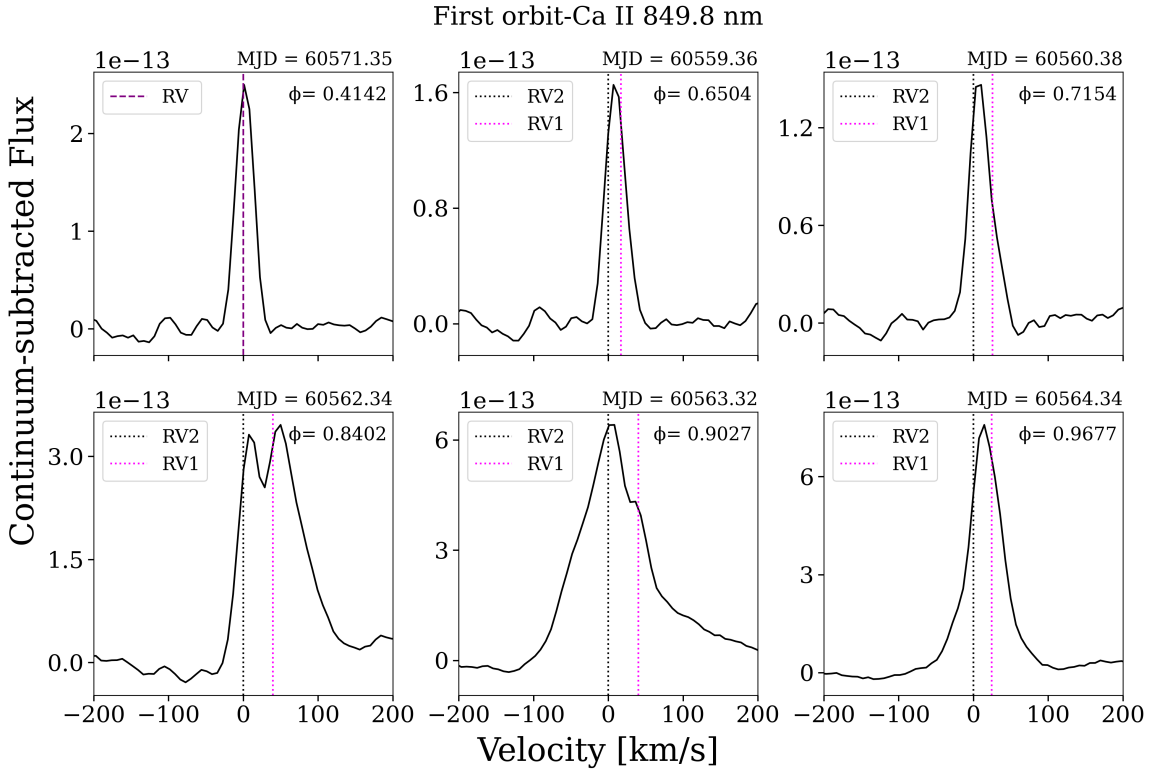


Fig. 8: X-Shooter/Ca II 849.8 nm continuum-subtracted line across the first orbital cycle. Orbital phase of each line is indicated in the upper right of each sub-figure. Magenta and black dotted lines show the RVs of the primary and secondary, respectively. Epochs with a single RV value (where $RV_1 = RV_2$) are shown with a purple dotted line. Lines are shifted to the rest-frame of the secondary.

3.2.2. Calcium emission line

We perform the removal of the photospheric absorption line and continuum subtraction locally around the Ca II 849.8 nm line by fitting each epoch with two or three Gaussian profiles and a linear component for the continuum. The second or third Gaussian component is used to account for the photospheric absorption around the emission line, when it is present, which must be removed to better trace the accretion of each star (Fig. 7). We then measure the flux of each Gaussian component readily from the continuum-subtracted flux-calibrated spectra.

In Fig. 8, Fig. 9, and 10, we show the residual Ca II 849.8 nm line in all the X-Shooter spectra in different orbits, centering the velocity scale on the secondary component. We infer that the primary/secondary is accreting the most when the highest peak velocity corresponds to the RV of one of them.

During the first orbital cycle (Fig. 8), DQ Tau accretes at all phases, including apastron ($\phi = 0.414$), but as it approaches the periastron $< 0.8402 < \phi < 0.9679$, we observe the line intensity becomes stronger as both stars are accreting with the secondary growing in flux, shown by the double-line feature of Ca II 849.8 nm line. However, the intensity of the primary emission line peak does not increase at the last two phases in the orbit compared to the secondary.

In the second to the seventh orbits (Fig. 9), we see that the secondary line intensity is stronger, possibly because it accretes more at $0.1274 < \phi < 0.2533$. While at $0.3055 < \phi < 0.5722$, we observe a single line with one RV tracing both components, i.e., hard to attribute the accretion to any of the stars. At the periastron, i.e., $\phi < 0.9367$, we observe that the two stars line intensities are lower with respect to the previous periastron phases. Finally, in the last two orbital cycles (Fig. 10), the Ca II 849.8 nm

line has the same line intensity approximately at and post periastron phases, indicating similar accretion rate.

The variability of the Ca II 849.8 nm double-line feature across the different orbits corresponds to the accretion variability of DQ Tau as indicated in the Fig. 1. The accretion of both stars is more strongly defined in the first orbital cycle.

To derive the accretion luminosity (L_{acc}) of each star, we use the calculated integrated flux for the Ca II 849.8 nm line at different phases for the primary and the secondary. This can only be done at the phases, where it is possible to distinguish the emission peaks of both stars. The derived flux across the orbital phase show how variable and modulated is the accretion of DQ Tau and that the secondary is contributing more to the measured flux of the Ca II 849.8 nm line. The flux ratio is elevated during the first orbital cycles at periastron, indicating that both stars are actively accreting. Different periastron passages bring variable flux ratios, confirming the variation of the strength of the accretion bursts as the epochs of the third and ninth orbits show lower values as shown in Fig. 1 and Fig. 11.

We derive L_{acc} for each star using the integrated flux values on the Ca II 849.8 nm line. We correct the derived flux for extinction at each epoch assuming an extinction value $A_V = 1.6$ mag and the Cardelli extinction law (Cardelli et al. 1989). The estimated reddening factor at $\lambda_{\text{Ca II 849.8 nm}}$ is ~ 0.45 . We first estimate the line luminosities $L_{\text{line},i}$ for each component scaling the flux for the distance as $L_{\text{line},i} = 4\pi d^2 F_{\text{line},i}$, where d is assumed to be 196 pc (Gaia Collaboration et al. 2023). The accretion luminosity is then derived using the relation:

$$\log(L_{\text{acc},i}) = a \cdot \log\left(\frac{L_{\text{line},i}}{L_{\odot}}\right) + b, \quad (7)$$

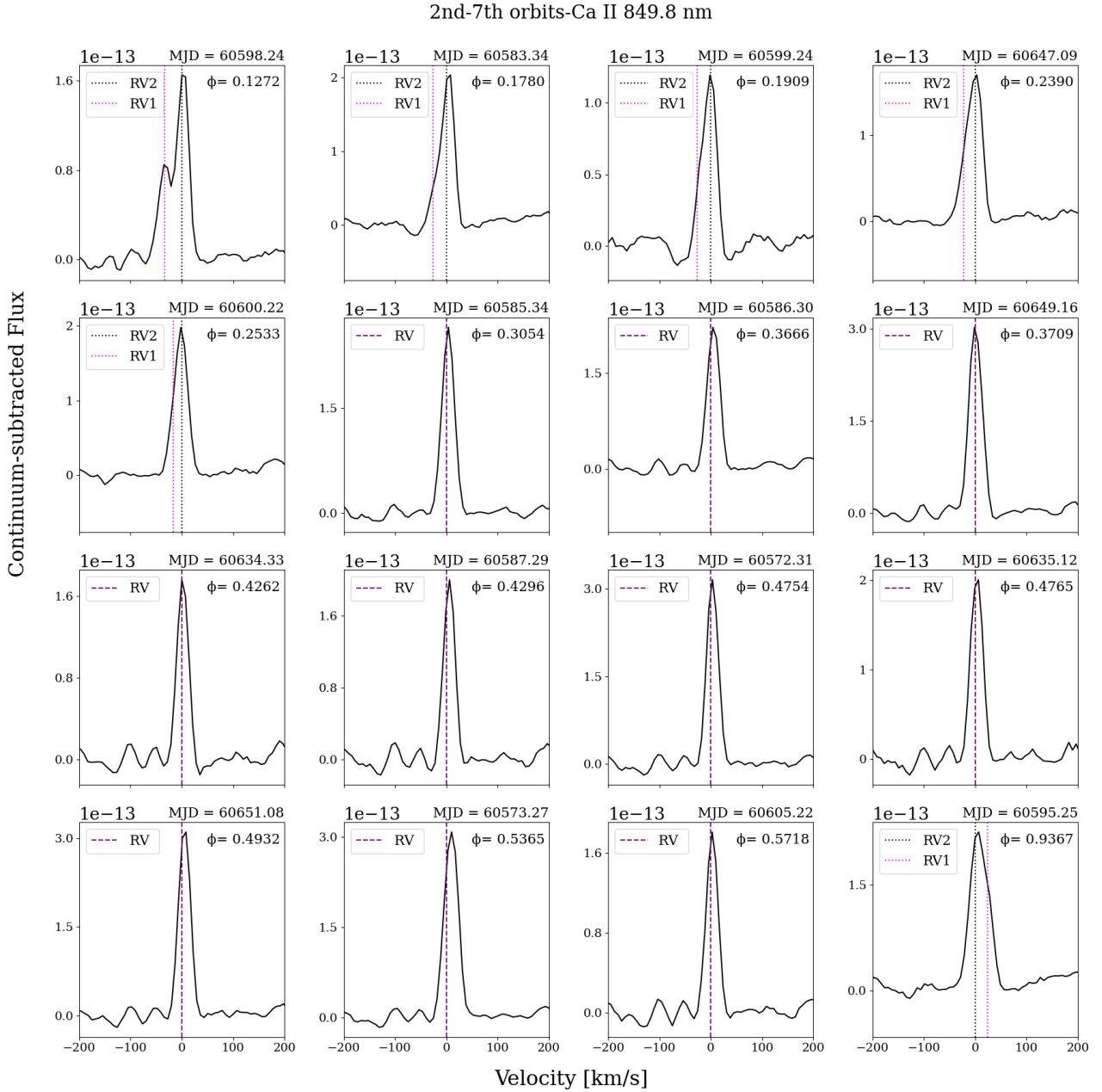


Fig. 9: X-Shooter/Ca II 849.8 nm continuum-subtracted line across the second to seventh orbits. Orbital phase of each line is indicated in the right upper part of each sub-figure. Magenta and black dotted lines indicate the RVs of primary and secondary, respectively. Epochs with one RV value correspond to epochs with single BF, where $RV_1 = RV_2$ are indicated with purple dotted line. The lines were shifted to the rest-frame of the secondary.

where the values for the a and b coefficients are 1.11 ± 0.13 and 3.71 ± 0.47 , as derived by Fiorellino et al. (2025). We assume an uncertainty of 0.2 dex on the disentangled L_{acc} . We note that the relations used here are calibrated using rmission line fluxes not corrected for the chromospheric contribution. Therefore, we do not correct for the chromospheric emission, which will be a considerable source of flux at the lowest accretion value

In Fig. 11, we compare the accretion luminosity derived from the integrated flux of Ca II 849.8 nm line to the values estimated by Tofflemire et al. (2025) from the UV-excess. We note that the latter assumed that the UV-excess traces the total accretion on the system. When the contribution to L_{acc} of each component is summed, the total value is in line with the values derived by Tofflemire et al. (2025) from the UV-excess. We disentangle the

accretion of the components at periastron $0.7 < \phi < 0.9$, and post-periastron phases $0.1 < \phi < 0.25$. At other phases, we derive one value of L_{acc} as the two components are fully blended.

The overall estimated L_{acc} follows the trend shown by Tofflemire et al. (2025), where DQ Tau appears in quiescent accretion mode until it approaches periastron. During the post periastron phases, the derived total luminosity values are in the same order of the epochs taken at apastron. The accretion luminosity values of each component across the phase show that the secondary is accreting at higher pace at post-periastron phases with evident difference in accretion near periastron. At periastron, different epochs from different DQ Tau orbital cycles show variable accretion of both stars. As shown by the Ca II 849.8 nm line peak emission, the primary accretes more during the burst in the first

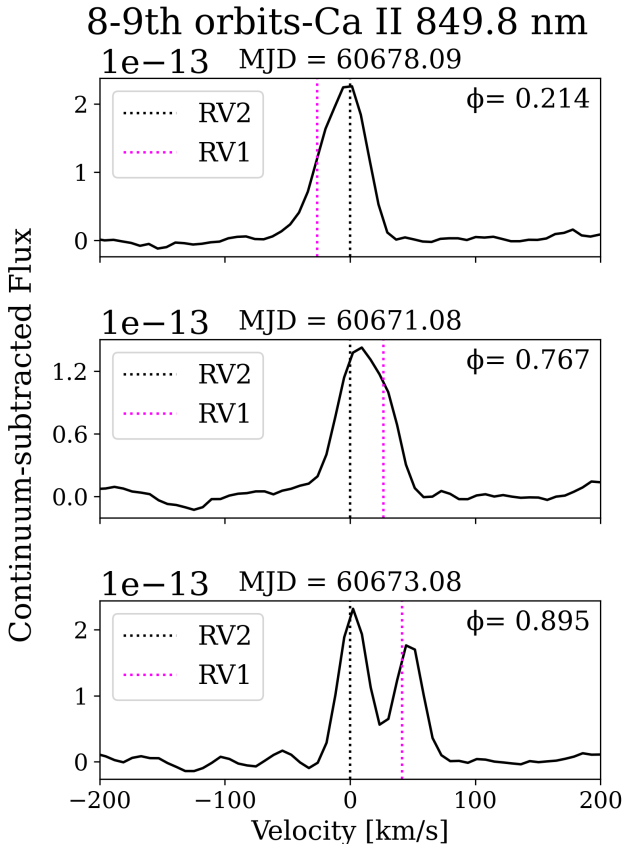


Fig. 10: X-Shooter/Ca II 849.8 nm continuum-subtracted line across the last orbital cycles. Orbital phase of each line is indicated in the upper right of each sub-figure. Magenta and black dotted lines show the RVs of the primary and secondary, respectively. Epochs with a single RV value (where $RV_1 = RV_2$) are shown with a purple dotted line. Lines are shifted to the rest-frame of the secondary.

orbit. The periastron phase during the third and ninth orbits show that the secondary is the dominant accretor during these bursts.

In Fig. B.1, we show that the relative veiling values for both components are tracing the accretion. The integrated flux, equivalent width, relative veiling, and L_{acc} values for all epochs are provided in Table E.1.

4. Discussion

4.1. Apsidal motion

The orbital properties of DQ Tau derived here, in particular the $e \sim 0.55$ and mass ratio $q \approx 0.97$, are in line with previously published papers on DQ Tau (e.g. Pouilly et al. 2024 and Czekala et al. 2016).

We report a prograde apsidal motion compared to Czekala et al. (2016). We fit $\omega = 263.1996^\circ \pm 0.0081$, instead of $231.9^\circ \pm 1.8$ (Czekala et al. 2016). We emphasize that this precession differs from that of the circumbinary disk cavity induced by the binary's quadrupole potential, which cannot be detected with present observations in DQ Tau but is nevertheless expected to occur on theoretical grounds (Ragusa et al. 2020; Penzlin et al. 2024).

The precession of the binary orbit could be explained by the gravitational influence of the disk on the binary parameters. Tiede et al. (2024) in their hydrodynamical simulation, showed

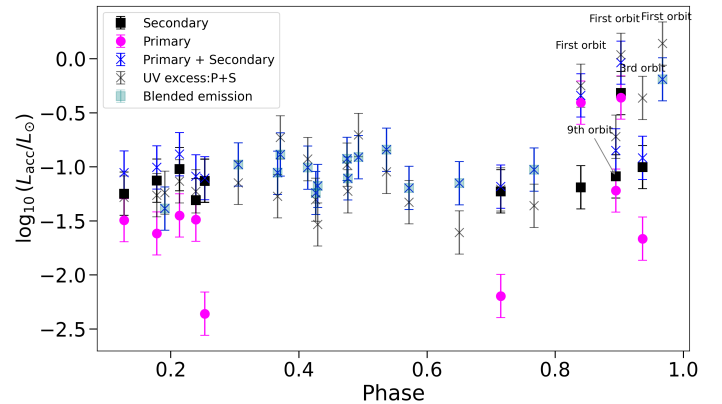


Fig. 11: X-Shooter/Ca II 849.8 nm accretion luminosity measured for each star in DQ Tau in comparison to Tofflemire et al. (2025) for DQ Tau as a single star. The sum of the total accretion luminosities for each component are in line with the values derived by Tofflemire et al. (2025). Blended epochs where we derive one integrated flux value are shown as light blue squares. The Secondary appears to dominate the accretion at the disentangled epochs. As DQ Tau approaches periastron, L_{acc} increases.

that an accreting eccentric binary experiences prograde apsidal precession faster than changes in the semi-major axis or eccentricity. Hence, the orientation of periastron shifts over time, which also affects the accretion behaviour across the orbit, periodically changing which component of the binary is the dominant accretor and causing significant variations in their individual accretion rates (Dunhill et al. 2015). Across 10 years, the resulted increment in the argument of periastron is $\Delta\omega \sim 30^\circ$. This means DQ Tau would complete one full precession cycle, with approximately 2770 orbits, over 120 years. As a first simplified approach to investigate the origin of the observed precession, we estimate the mass that a putative third body in the system would need to reproduce it. We use the approximation by Murray & Dermott (1999) to estimate the mass of this putative companion. First, we define the apsidal precession rate as :

$$\dot{\omega} \simeq \frac{3}{4} \frac{M_{\text{out}}}{M_{\text{bin}}} \left(\frac{a_{\text{bin}}}{a_{\text{out}}} \right)^3 \Omega_{\text{bin}} , \quad (8)$$

where M_{out} is the mass of the external companion, M_{bin} is the binary mass, a_{bin} is the binary semi-major axis, a_{out} is the semi-major axis of the external companion, and Ω_{bin} is the binary mean motion. Then, we consider the binary precession timescale compared to the binary orbital scale :

$$t_{\text{prec}} = \frac{\Omega_{\text{bin}}}{\dot{\omega}} = \frac{4}{3} \left(\frac{a_{\text{out}}}{a_{\text{bin}}} \right)^3 \frac{M_{\text{bin}}}{M_{\text{out}}} , \quad (9)$$

Eq. 9 reduces to the following :

$$M_{\text{out}} = \frac{4}{3} \left(\frac{a_{\text{out}}}{a_{\text{bin}}} \right)^3 \frac{M_{\text{bin}}}{t_{\text{prec}}/t_{\text{bin}}} , \quad (10)$$

which describes the relation between the mass and semi-major axis that a putative companion should have in order to explain the observed precession rate. For DQ Tau, we estimate the mass range of a putative companion responsible for the observed precession rate between $15M_J$ at the cavity edge ($\sim 3a_{\text{bin}}$) and

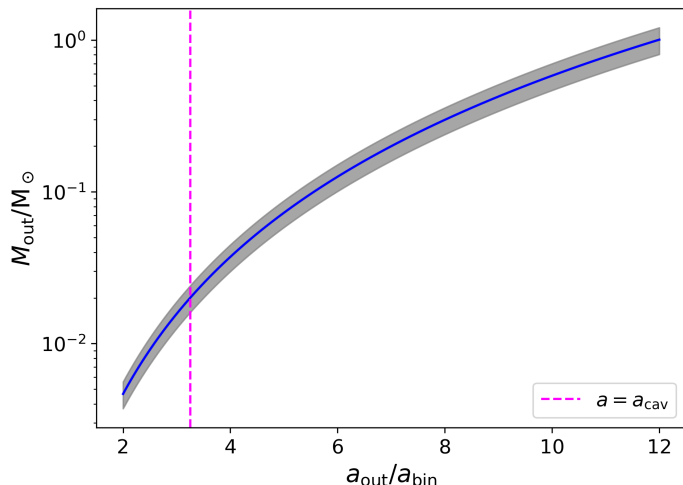


Fig. 12: Mass of a putative third companion as a function of its orbital separation relative to the binary, required to reproduce the observed apsidal precession of DQ Tau. The solid blue curve shows the corresponding mass estimate, the grey shaded area indicates the uncertainty range, and the vertical magenta dashed line marks the predicted cavity radius ($\sim 3a_{\text{bin}}$), based on DQ Tau orbital properties and assuming a circular coplanar disk (Ragusa et al. 2025).

1 M_{\odot} at a separation of $\sim 12a_{\text{bin}}$ (Fig.12). The latter would have been detected, if existed, as it would disturb the disk and carve a cavity. The dust disk mass of DQ Tau is derived to be $75M_{\oplus}$ (Manara et al. 2023) based on the ALMA data by Long et al. (2019). Assuming a gas-to-dust ratio of 100, the disk mass would be $\sim 25M_J$, resulting in a ratio of ~ 0.02 compared to its total $M_{\text{bin}} \sim 1.21M_{\odot}$. This implies that the precession timescale of DQ Tau could be explained by the disk as shown by Ragusa et al. (2018), where they modelled the effect of the disk on the precession of the inner companion as an effective additional planet in the system.

4.2. Accretion rate modulation

Using the Ca II 849.8 nm line and the relative line veiling due to spots and accretion, as measured from the Li 670.8 nm line, we provided detailed phase-resolved characterisations of accretion onto the individual components in DQ Tau. While the primary star appears to accrete more at the periastron phases, the secondary star dominates at post periastron passage. Both stars strongly accrete near the periastron in the first orbit. The derived L_{acc} of each component shows that the accretion onto the primary star is ~ 1.5 dex higher at periastron compared to the previous quiescent state phases.

In our analysis, we observe DQ Tau accreting at all phases, including at apastron. Many previous works (Tofflemire et al. 2017a; Pouilly et al. 2023, 2024) also observed accretion events at apastron. Bary & Petersen (2014) observed an anomalous flare at apastron ($\phi = 0.372$ and $\phi = 0.433$) with a mass accretion rate that is an order of magnitude stronger than the quiescent rate. This was interpreted due to perturbations in the circumbinary disk, leading to the formation of irregularly shaped, non-axisymmetric structures extending inward from the inner edge of the disk as shown by simulations of Günther & Kley (2002). The presence of such structures coinciding with the close passage of one or both stars at apastron, may have led to that unique

accretion flare. In our data, we observe an elevated L_{acc} at apastron as the binary is closest to the cavity edge and strip more material.

Our results are in line with to Fiorellino et al. (2022a) , in which they covered two epochs of each of the four orbital cycles studied. They reported that the primary was the dominant accretor at the periastron passage and at others was the secondary. The main accretor in their data also changed depending on which accretion line tracer was considered. This phase-dependent switching occurred because different lines originate in different regions in the accretion columns such that new material was accreting onto one star while older material is still accreting onto the other.

Pouilly et al. (2023) used different accretion tracers like $H\alpha$, $H\beta$, $H\gamma$, Ca II and the narrow component of HeI 5876Å line, and reported that the secondary component was the main accretor. However, in a subsequent work (Pouilly et al. 2024), they concluded that the accretion behavior of the DQ Tau components seemed to be balanced. This was interpreted as the result of the evolution of the primary large-scale magnetic field. In both papers, ESPaDOnS data were taken with time gap of ~ 2 years. This alternating accretion behavior was also observed by Fiorellino et al. (2022a), using data taken between 2012-2013. Building on these results, our observing campaign shows that the accretion behavior of DQ Tau is very complex. The primary and the secondary components are actively accreting near the several periastron passages, while the secondary star is the strongest accretor during the other phases. The several orbits coverage illustrates that the variability in which component dominates in accretion strength and in the overall accretion intensity is extremely time-dependent, confirming the necessity to monitor for longer time close binary systems like DQ Tau to better constrain models of accretion in binary systems. Furthermore, in equal-mass binary star systems as DQ Tau, accretion is characterised by the variability of material arriving through the tidal streams from the edge of the cavity.

In summary, tracing the accretion pattern of DQ Tau over the past decade has shown a fluctuating pattern between periods of balanced accretion and times when either the primary or secondary star dominates the accretion process. Building upon previous research, our multi-orbit campaign demonstrates that DQ Tau accretion behavior is highly variable over time, with the intensity of accretion activity and the leading accretor changing from one orbit to another. This accretion variability changes the inner disk properties, in particular its temperature, which affect the chemistry and the process of forming planets, as shown by (Poblete et al. 2025). The availability of this information on the binary interaction is of paramount importance to interpret the JWST molecular emission data obtained for DQ Tau.

5. Conclusions

In this work we calculated the radial velocity of the two components of DQ Tau across four months, about 10 orbits, using X-Shooter and UVES spectra. We derived the orbital parameters of the system. Using the integrated flux of the Ca II 849.8 nm, we measured the accretion luminosity on each component across the orbital phases.

We conclude the following:

- The orbital solution we provide is in agreement with previously published results, i.e., Pouilly et al. (2024).
- We report prograde apsidal motion, which could be caused by the disk, acting as a third body in the system.

- Alternatively, we explore the influence of a third body interacting with the binary and causing the observed precession. Such object should have a mass of at least $\sim 15M_J$ at a separation of $\sim 3a_{\text{bin}}$.
- By analysing the accretion lines using only the Ca II triplet, we were able to trace the accretion of both stars. We confirm that the primary and secondary stars accrete differently across the phase and that they alternate in the accretion dominance at periastron.
- The summed values derived from disentangling accretion on each component are in line with the global values measured by Tofflemire et al. (2025) using the UV-excess on the unresolved spectra of DQ Tau.

The values of the orbit and of the accretion rates derived in this work should be used for the analysis of the JWST spectra of DQ Tau obtained at the time of the observations described here, as well as those obtained shortly after (Kóspál et al. 2025). A modeling of the properties of the inner disk of this complex system should be carried out considering both the orbital dynamics and the accretion rate variability derived in this work. Similar coordinated ground- and space-based observing campaigns should be set up for future studies of time-variable inner disk chemical properties.

Acknowledgements. We thank the anonymous referee for their useful report. We thank Myriam Benisty, Cathie Clarke, and Jeff Bary for insightful discussions. Funded by the European Union under the European Union’s Horizon Europe Research & Innovation Programme 101039452 (WANDA). EF has received funding from the European Research Council (ERC) via the ERC Synergy Grant ECOGAL (grant 855130). Views and opinions expressed are, however, those of the author(s) only and do not necessarily reflect those of the European Union or the European Research Council. Neither the European Union nor the granting authority can be held responsible for them. ER acknowledges financial support from the European Union’s Horizon Europe research and innovation programme under the Marie Skłodowska-Curie grant agreement No. 101102964 (ORBIT-D), including a secondment carried out at the ESO Headquarters in Garching, Germany.

References

Artymowicz, P. & Lubow, S. H. 1996, *ApJ*, 467, L77

Bae, J., Isella, A., Zhu, Z., et al. 2023, in Astronomical Society of the Pacific Conference Series, Vol. 534, Protostars and Planets VII, ed. S. Inutsuka, Y. Aikawa, T. Muto, K. Tomida, & M. Tamura, 423

Ballester, P., Modigliani, A., Boitquin, O., et al. 2000, *The Messenger*, 101, 31

Banzatti, A., Pontoppidan, K. M., Pérez Chávez, J., et al. 2023, *AJ*, 165, 72

Bary, J. S. & Petersen, M. S. 2014, *ApJ*, 792, 64

Bate, M. R. 2000, in American Astronomical Society Meeting Abstracts, Vol. 197, American Astronomical Society Meeting Abstracts, 10.04

Benisty, M., Dominik, C., Follette, K., et al. 2023, in Astronomical Society of the Pacific Conference Series, Vol. 534, Protostars and Planets VII, ed. S. Inutsuka, Y. Aikawa, T. Muto, K. Tomida, & M. Tamura, 605

Biller, B., Lacour, S., Juhász, A., et al. 2012, *ApJ*, 753, L38

Campbell-White, J., Manara, C. F., Sicilia-Aguilar, A., et al. 2023, *A&A*, 673, A80

Campbell-White, J., Sicilia-Aguilar, A., Manara, C. F., et al. 2021, *MNRAS*, 507, 3331

Cardelli, J. A., Clayton, G. C., & Mathis, J. S. 1989, *ApJ*, 345, 245

Czekala, I., Andrews, S. M., Torres, G., et al. 2016, *ApJ*, 818, 156

Dekker, H., D’Odorico, S., Kaufer, A., Delabre, B., & Kotzlowski, H. 2000, in Society of Photo-Optical Instrumentation Engineers (SPIE) Conference Series, Vol. 4008, Optical and IR Telescope Instrumentation and Detectors, ed. M. Iye & A. F. Moorwood, 534–545

Dunhill, A. C., Cuadra, J., & Dougados, C. 2015, *MNRAS*, 448, 3545

Fiorellino, E., Alcalá, J. M., Manara, C. F., et al. 2025, arXiv e-prints, arXiv:2509.21078

Fiorellino, E., Park, S., Kóspál, Á., & Ábrahám, P. 2022a, *ApJ*, 928, 81

Fiorellino, E., Zsidi, G., Kóspál, Á., et al. 2022b, *ApJ*, 938, 93

Fischer, W. J., Hillenbrand, L. A., Herczeg, G. J., et al. 2023, in Astronomical Society of the Pacific Conference Series, Vol. 534, Protostars and Planets VII, ed. S. Inutsuka, Y. Aikawa, T. Muto, K. Tomida, & M. Tamura, 355

Frasca, A., Boffin, H. M. J., Manara, C. F., et al. 2021, *A&A*, 656, A138

Freudling, W., Romaniello, M., Bramich, D. M., et al. 2013, *A&A*, 559, A96

Gaia Collaboration, Vallenari, A., Brown, A. G. A., et al. 2023, *A&A*, 674, A1

Gómez de Castro, A. I., López-Santiago, J., Talavera, A., Sytov, A. Y., & Bisikalo, D. 2013, *ApJ*, 766, 62

Grant, S. L., van Dishoeck, E. F., Tabone, B., et al. 2023, *ApJ*, 947, L6

Günther, R. & Kley, W. 2002, *A&A*, 387, 550

Hartmann, L., Herczeg, G., & Calvet, N. 2016, *ARA&A*, 54, 135

Ireland, M. J. & Kraus, A. L. 2008, *ApJ*, 678, L59

Keppler, M., Penzlin, A., Benisty, M., et al. 2020, *A&A*, 639, A62

Kóspál, Á., Ábrahám, P., Akimkin, V. V., et al. 2025, arXiv e-prints, arXiv:2508.19701

Long, F., Herczeg, G. J., Harsono, D., et al. 2019, *ApJ*, 882, 49

Manara, C. F., Ansdell, M., Rosotti, G. P., et al. 2023, in Astronomical Society of the Pacific Conference Series, Vol. 534, Protostars and Planets VII, ed. S. Inutsuka, Y. Aikawa, T. Muto, K. Tomida, & M. Tamura, 539

Manara, C. F., Frasca, A., Venuti, L., et al. 2021, *A&A*, 650, A196

Manara, C. F., Testi, L., Rigliaco, E., et al. 2013, *A&A*, 551, A107

Mathieu, R. D., Stassun, K., Basri, G., et al. 1997, *AJ*, 113, 1841

Modigliani, A., Goldoni, P., Royer, F., et al. 2010, in Society of Photo-Optical Instrumentation Engineers (SPIE) Conference Series, Vol. 7737, Observatory Operations: Strategies, Processes, and Systems III, ed. D. R. Silva, A. B. Peck, & B. T. Soifer, 773728

Muñoz, D. J. & Lai, D. 2016, *ApJ*, 827, 43

Murray, C. D. & Dermott, S. F. 1999, *Solar System Dynamics*

Nowak, M., Rowther, S., Lacour, S., et al. 2024, *A&A*, 683, A6

Penzlin, A. B. T., Booth, R. A., Nelson, R. P., Schäfer, C. M., & Kley, W. 2024, *MNRAS*, 532, 3166

Poblete, P. P., Cuello, N., Alaguero, A., et al. 2025, arXiv e-prints, arXiv:2509.12898

Pouilly, K., Hahlin, A., Kochukhov, O., Morin, J., & Kóspál, Á. 2024, *MNRAS*, 528, 6786

Pouilly, K., Kochukhov, O., Kóspál, Á., et al. 2023, *MNRAS*, 518, 5072

Ragusa, E., Alexander, R., Calcino, J., Hirsh, K., & Price, D. J. 2020, *MNRAS*, 499, 3362

Ragusa, E., Lodato, G., Cuello, N., et al. 2025, *A&A*, 698, A102

Ragusa, E., Lodato, G., & Price, D. J. 2016, *MNRAS*, 460, 1243

Ragusa, E., Rosotti, G., Teyssandier, J., et al. 2018, *MNRAS*, 474, 4460

Smette, A., Sana, H., Noll, S., et al. 2015, *A&A*, 576, A77

Stelzer, B., Frasca, A., Alcalá, J. M., et al. 2013, *A&A*, 558, A141

Teyssandier, J. & Lai, D. 2020, *MNRAS*, 495, 3920

Tiede, C., D’Orazio, D. J., Zwick, L., & Duffell, P. C. 2024, *ApJ*, 964, 46

Toci, C., Ceppi, S., Cuello, N., et al. 2024, *A&A*, 688, A102

Tofflemire, B. M., Manara, C. F., Banzatti, A., et al. 2025, arXiv e-prints, arXiv:2504.08029

Tofflemire, B. M., Mathieu, R. D., Ardila, D. R., et al. 2017a, *ApJ*, 835, 8

Tofflemire, B. M., Mathieu, R. D., Herczeg, G. J., Akeson, R. L., & Ciardi, D. R. 2017b, *ApJ*, 842, L12

Tofflemire, B. M., Mathieu, R. D., & Johns-Krull, C. M. 2019, *AJ*, 158, 245

Tokovinin, A. A. 2000, *A&A*, 360, 997

Verhoeff, A. P., Min, M., Pantin, E., et al. 2011, *A&A*, 528, A91

Vernet, J., Dekker, H., D’Odorico, S., et al. 2011, *A&A*, 536, A105

Young, M. D., Baird, J. T., & Clarke, C. J. 2015, *MNRAS*, 447, 2907

Zsidi, G., Fiorellino, E., Kóspál, Á., et al. 2022, *ApJ*, 941, 177

Appendix A: RV fit and broadening functions

The fit of the RV curve described in Sect. 3.1 is performed with an MCMC tool, which allows one to explore the correlation between the posterior distribution of the fitted values. This is shown in Fig. A.1. The distributions are single-peaked, with Gaussian profiles. The magenta lines in Fig. A.1 highlight the location of the best likelihood estimates. The off-diagonal 2D plots represent the bivariate distributions between each pair of parameters which provide an immediate estimate of their correlation. Additional plots of the BF and of the dependence of RV with wavelength (Fig. A.2) are shown here.

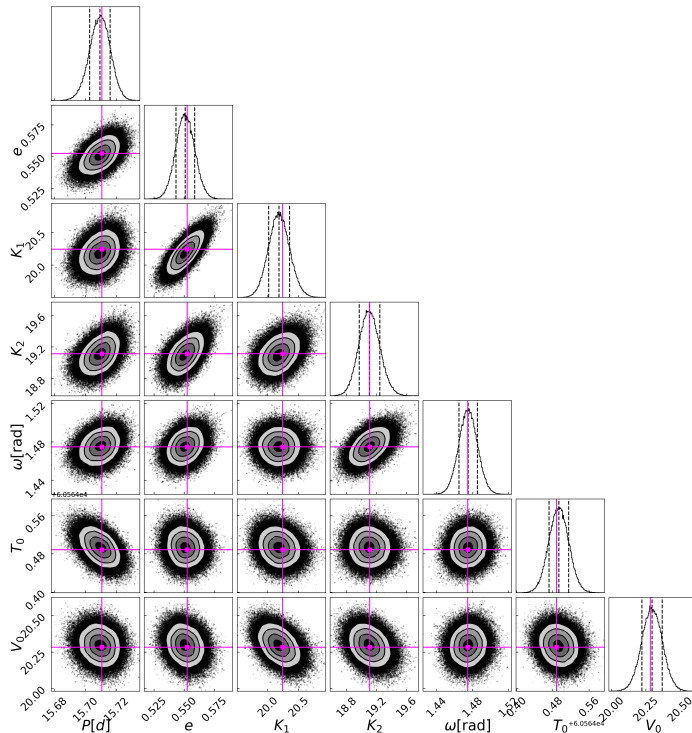


Fig. A.1: Corner plot of the orbital solution for DQ Tau. The vertical dashed lines indicating the 16th, 50th and 84th percentile. The vertical magenta lines correspond to the best likelihood estimates of each distribution.

Appendix B: Changes in relative veiling and relation with accretion

Measuring the veiling of each individual component of a spectroscopic binary system is not trivial (e.g. Tofflemire et al. 2019). Indeed, in a combined light spectrum the additional continuum due to accretion makes the absorption lines shallower with respect to the combined continuum. This additional continuum, however, affects absorption lines from both the primary and secondary equally, regardless of which star it is coming from. The variations observed here in the EW values could thus be caused by both veiling and/or by spots (e.g. Bary & Petersen 2014) or rotational modulation.

In order to test whether the EW variations we see are related to accretion, we plot in Fig. B.1 the measured L_{acc} for the primary and secondary stars, derived from the Ca II 849.8 nm line, as a function of the relative veiling factor measured from the Li 670.8 nm line. We see that the observed variations of veiling in both components of the line suggest that the relative veiling variations are mainly tracing the accretion variability in DQ Tau.

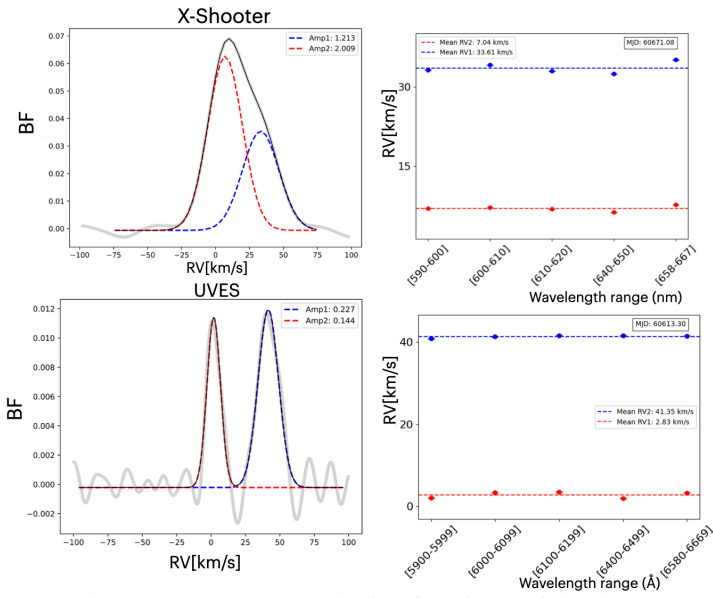


Fig. A.2: X-Shooter and UVES broadening functions. Right, the calculated RVs across one spectrum for each spectrograph. The dotted lines represent the mean values.

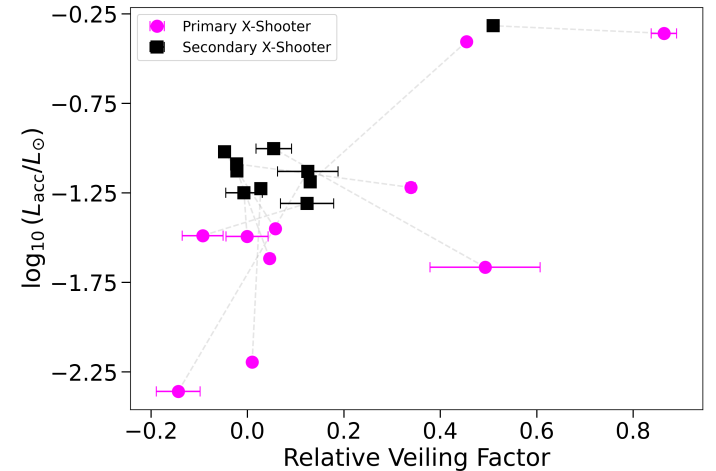


Fig. B.1: Accretion luminosity L_{acc} of the primary and secondary stars as a function of the relative veiling. The dotted lines connects the two stars of each epoch, allowing direct comparison of their accretion activity. The data follows a trend, where higher veiling factors are generally associated with larger L_{acc} .

Appendix C: X-Shooter and UVES/HeI 587.56 emission line

We show here the He I 587.56 nm line observed across the first, middle, and last orbital cycles of DQ Tau in the X-Shooter and UVES data (Fig. C.1-C.3).

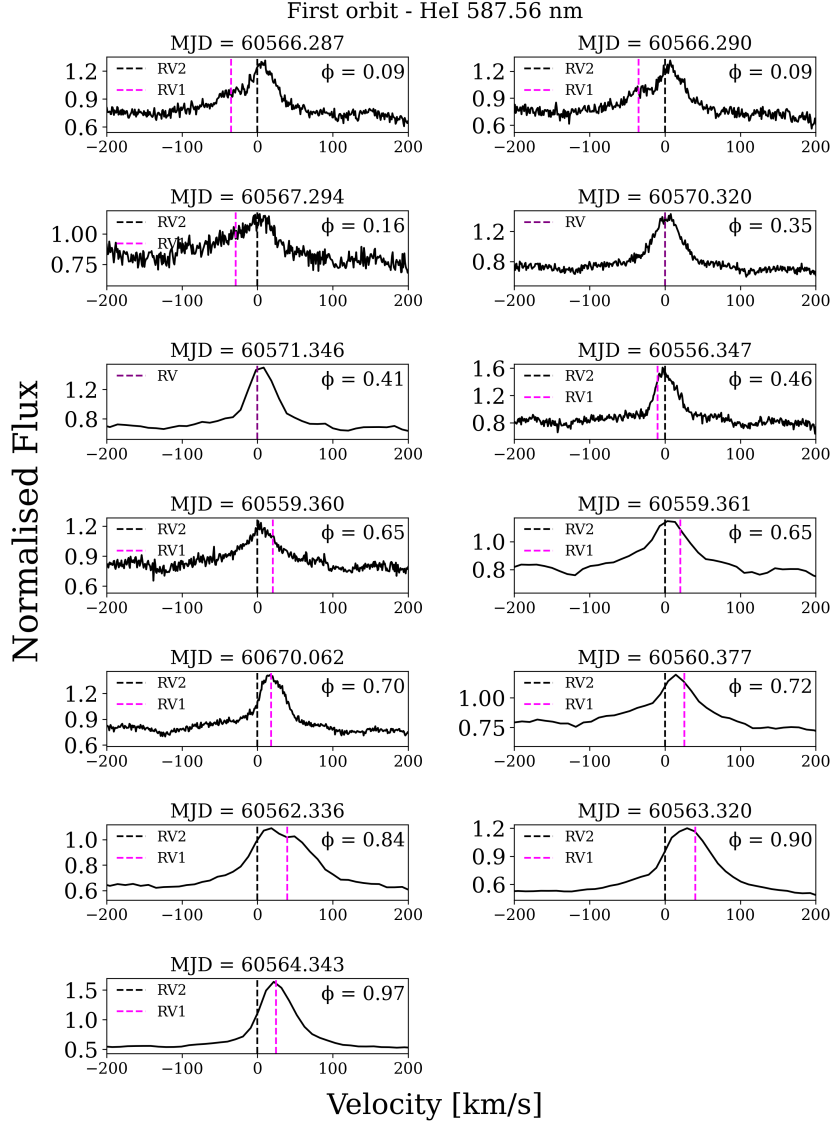


Fig. C.1: X-Shooter and UVES/HeI 587.56 nm line across the first orbit covered by this dataset. The orbital phase of each line is indicated in the right upper part of each sub-figure. The magenta and black dotted lines indicate the RVs of primary and secondary, respectively. Epochs with single RV value correspond to those with a single narrow-peaked BF ($RV_1 = RV_2$) are indicated with purple dotted line. Lines are shifted to the rest-frame of the secondary.

Last orbit - HeI 587.56 nm

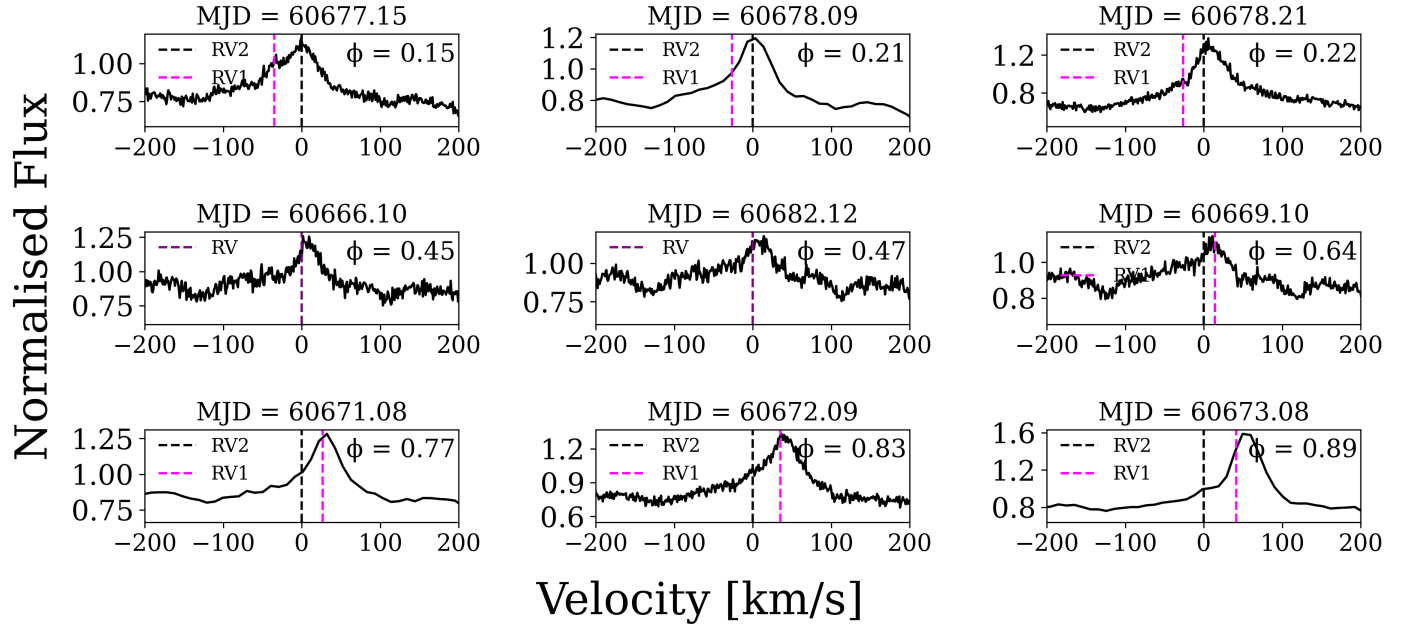


Fig. C.2: X-Shooter and UVES/HeI 587.56 nm line across the last two orbits covered by this dataset. The orbital phase of each line is indicated in the right upper part of each sub-figure. The magenta and black dotted lines indicate the RVs of the primary and secondary, respectively. Epochs with single RV value correspond to those with a single narrow-peaked BF ($RV_1 = RV_2$) are indicated with purple dotted line. Lines are shifted to the rest-frame of the secondary.

2nd-7th orbits - HeI 587.56 nm

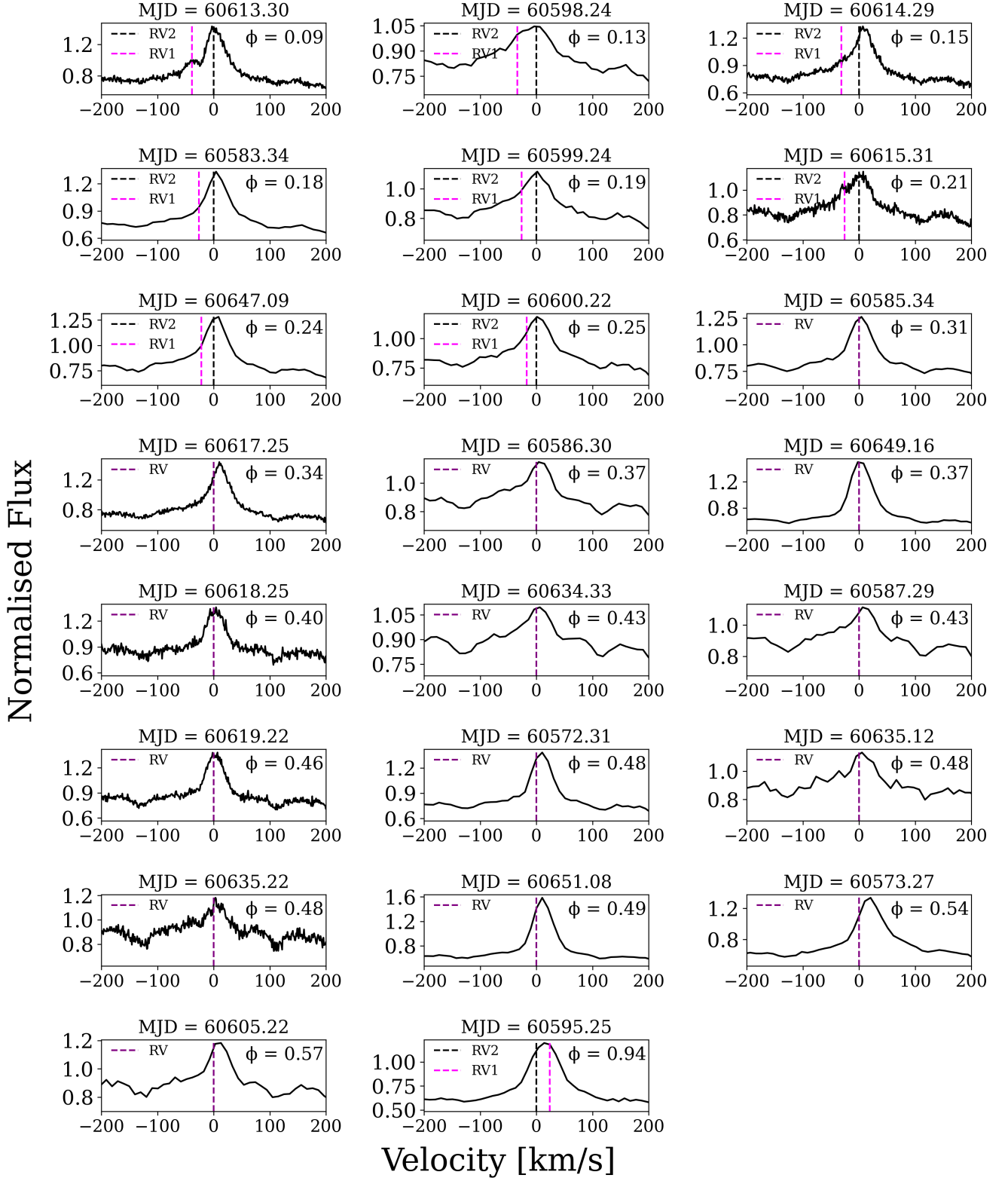


Fig. C.3: X-Shooter and UVES/HeI 587.56 nm line across the middle orbital cycles. The orbital phase of each line is indicated in the right upper part of each sub-figure. The magenta and black dotted lines indicate the RVs of primary and secondary, respectively. Epochs with single RV value correspond to those with a single narrow-peaked BF ($RV_1 = RV_2$) are indicated with purple dotted line. Lines are shifted to the rest-frame of the secondary.

Appendix D: Log of observations

Table D.1: Log of the observations, radial velocity measurements and S/N of the reduced spectra for each spectrograph.

Spectrograph	MJD	Obs date	RV_1	σ_1	RV_2	σ_2	S/N
UVES	60556.3473	2024-09-03T08:20:02.582	19.472	1.339	29.448	1.017	13.08
UVES	60559.3603	2024-09-06T08:38:45.925	36.564	4.739	16.265	2.474	15.63
X-Shooter	60559.3611	2024-09-06T08:39:58.340	25.534	1.923	8.485	1.453	43.43
X-Shooter	60560.3768	2024-09-07T09:02:34.464	30.655	1.779	4.995	1.193	48.87
X-Shooter	60562.3363	2024-09-09T08:04:18.219	40.453	0.000	0.703	0.284	62.28
X-Shooter	60563.3197	2024-09-10T07:40:19.868	40.368	0.169	0.169	0.502	76.71
X-Shooter	60564.3425	2024-09-11T08:13:13.816	32.325	0.745	7.721	2.727	68.50
UVES	60566.2867	2024-09-13T06:52:46.690	3.703	0.425	38.787	0.176	30.52
UVES	60566.2901	2024-09-13T06:57:46.067	3.619	0.305	38.593	0.201	11.33
UVES	60567.2944	2024-09-14T07:03:58.888	6.159	0.878	35.036	0.662	10.27
UVES	60570.3200	2024-09-17T07:40:45.505	-	-	23.578	0.203	16.45
X-Shooter	60571.3463	2024-09-18T08:18:39.848	-	-	20.406	0.481	37.33
X-Shooter	60572.3054	2024-09-19T07:19:43.649	-	-	18.288	0.427	36.43
X-Shooter	60573.2743	2024-09-20T06:35:02.610	-	-	18.371	0.578	39.41
X-Shooter	60583.3431	2024-09-30T08:14:02.391	6.514	1.904	32.724	0.892	50.76
X-Shooter	60585.3402	2024-10-02T08:09:54.165	-	-	22.009	0.500	41.12
X-Shooter	60586.3031	2024-10-03T07:16:27.712	-	-	21.982	0.376	37.82
X-Shooter	60587.2900	2024-10-04T06:57:35.924	-	-	19.578	0.441	34.67
X-Shooter	60595.2489	2024-10-12T05:58:20.894	33.540	1.968	9.724	1.284	55.14
X-Shooter	60598.2419	2024-10-15T05:48:23.514	2.633	1.237	36.726	0.958	50.22
X-Shooter	60599.2394	2024-10-16T05:44:41.765	4.623	1.146	30.939	0.766	46.77
X-Shooter	60600.2194	2024-10-17T05:15:56.614	13.827	2.895	31.118	0.716	45.92
X-Shooter	60605.2246	2024-10-22T05:23:27.302	-	-	17.526	0.769	36.54
UVES	60613.3049	2024-10-30T07:18:59.902	2.828	0.685	41.352	0.265	23.86
UVES	60614.2878	2024-10-31T06:54:23.536	4.464	0.788	35.974	0.232	27.89
UVES	60615.3078	2024-11-01T07:23:14.125	6.717	0.963	32.555	0.294	26.92
UVES	60617.2498	2024-11-03T05:59:43.470	-	-	22.100	0.163	28.74
UVES	60618.2521	2024-11-04T06:03:04.510	-	-	22.771	0.313	17.34
UVES	60619.2213	2024-11-05T05:18:39.420	-	-	22.383	0.156	25.27
X-Shooter	60634.3325	2024-11-20T07:58:46.090	-	-	20.896	0.453	35.48
X-Shooter	60635.1223	2024-11-21T02:56:03.098	-	-	21.725	0.513	33.16
UVES	60635.2244	2024-11-21T05:23:09.887	-	-	22.021	0.258	22.18
X-Shooter	60647.0948	2024-12-03T02:16:30.919	10.631	1.728	32.713	0.830	47.57
X-Shooter	60649.1622	2024-12-05T03:53:31.891	-	-	21.950	0.587	44.46
X-Shooter	60651.0810	2024-12-07T01:56:37.127	-	-	18.661	0.605	40.59
UVES	60666.1012	2024-12-22T02:25:46.064	-	-	21.545	0.150	6.04
UVES	60669.1003	2024-12-25T02:24:25.592	27.483	0.710	13.235	0.685	27.63
UVES	60670.0615	2024-12-26T01:28:34.295	29.198	1.797	11.105	0.951	30.09
X-Shooter	60671.0782	2024-12-27T01:52:37.461	33.613	0.940	7.036	0.460	48.45
UVES	60672.0943	2024-12-28T02:15:45.179	39.173	1.088	3.726	0.611	17.24
X-Shooter	60673.0831	2024-12-29T01:59:35.525	40.367	0.172	-1.125	0.425	57.79
UVES	60677.1474	2025-01-02T03:32:12.340	4.681	0.503	39.379	0.285	27.85
X-Shooter	60678.0910	2025-01-03T02:11:02.833	6.362	0.996	32.607	0.618	50.83
UVES	60678.2086	2025-01-03T05:00:23.899	6.139	0.568	32.354	0.193	18.88
UVES	60682.1153	2025-01-07T02:46:01.030	-	-	21.976	0.173	20.61

Notes. The RV values of both components are calculated using the BF technique on X-Shooter and UVES spectra. Dashed RV_1 values correspond to the epochs, where we can not distinguish the RV signature of both components. Therefore, we assume $RV_1 = RV_2$, i.e, the BF is single and narrow-peaked. In these cases, RV_1 values were assumed with higher errors compared to RV_2 values.

Appendix E: Table of derived fluxes, equivalent widths, relative veiling factors, and accretion luminosities

Table E.1: Derived integrated flux, equivalent width, relative veiling factor, and $\log\left(\frac{L_{acc}}{L_\odot}\right)$ for each epoch.

MID	$F_1\left[\frac{\text{erg}}{\text{cm}^2\text{s}}\right]$	$F_2\left[\frac{\text{erg}}{\text{cm}^2\text{s}}\right]$	$F_{\text{total}}\left[\frac{\text{erg}}{\text{cm}^2\text{s}}\right]$	$EW_1\left[\mu\text{m}\right]$	$EW_2\left[\mu\text{m}\right]$	$\sigma_{EW_1}\left[10^{-3}\text{ nm}\right]$	$\sigma_{EW_2}\left[10^{-3}\text{ nm}\right]$	VF_1	VF_2	σ_{VF_1}	σ_{VF_2}	$\log\left(\frac{L_{acc,1}}{L_\odot}\right)$	$\log\left(\frac{L_{acc,2}}{L_\odot}\right)$	$\log\left(\frac{L_{acc,\text{total}}}{L_\odot}\right)$
60559.361	-	-	1.580e-14	0.03	0.03	3.97	3.03	-0.13	0.07	0.13	0.11	-	-1.15	-1.15
60560.377	1.810e-15	1.350e-14	1.531e-14	0.02	0.03	0.18	0.16	0.01	0.03	0.01	0.01	-2.20	-1.23	-1.18
60562.336	7.420e-14	1.460e-14	8.88e-14	0.02	0.03	0.07	0.05	0.45	0.13	0.01	0.00	-0.41	-1.19	-0.34
60563.320	8.170e-14	8.920e-14	1.709e-13	0.01	0.02	0.18	0.17	0.86	0.51	0.03	0.01	-0.36	-0.32	-0.04
60564.343	-	-	1.160e-13	0.02	0.01	1.01	0.93	0.13	1.27	0.06	0.15	-	-	-0.19
60571.346	-	-	2.130e-14	0.02	0.03	0.03	0.03	0.00	0.08	0.00	0.00	-	-	-1.01
60572.305	-	-	2.520e-14	0.02	0.03	0.00	0.00	0.00	0.02	0.00	0.00	-	-	-0.93
60573.274	-	-	3.000e-14	0.02	0.03	0.04	0.04	0.00	0.09	0.00	0.00	-	-	-0.84
60583.343	6.020e-15	1.660e-14	2.262e-14	0.02	0.03	0.19	0.19	0.05	-0.02	0.01	0.01	-1.62	-1.13	-1.01
60585.340	-	-	2.260e-14	0.02	0.03	0.01	0.01	0.00	0.12	0.00	0.00	-	-	-0.98
60586.303	-	-	1.930e-14	0.02	0.03	0.00	0.00	0.00	-0.01	0.00	0.00	-	-	-1.06
60587.290	-	-	1.500e-14	0.02	0.03	0.00	0.00	0.00	-0.05	0.00	0.00	-	-	-1.18
60595.249	5.440e-15	2.150e-14	2.694e-14	0.02	0.03	1.20	1.05	0.49	0.05	0.11	0.04	-1.67	-1.00	-0.92
60598.242	7.760e-15	1.290e-14	2.060e-14	0.02	0.03	1.03	1.22	-0.00	-0.01	0.04	0.04	-1.49	-1.25	-1.05
60599.239	-	-	9.700e-15	0.02	0.03	0.70	0.76	0.00	-0.05	0.03	0.02	-	-	-1.39
60600.219	1.290e-15	1.650e-14	1.779e-14	0.03	0.03	1.45	1.57	-0.14	0.13	0.05	0.06	-2.36	-1.13	-1.11
60605.225	-	-	1.440e-14	0.02	0.03	0.04	0.04	0.00	0.00	0.00	0.00	-	-	-1.20
60634.332	-	-	1.310e-14	0.02	0.03	0.05	0.05	0.00	-0.03	0.00	0.00	-	-	-1.24
60635.122	-	-	1.730e-14	0.02	0.03	0.02	0.02	0.00	-0.05	0.00	0.00	-	-	-1.11
60647.095	7.840e-15	1.140e-14	1.924e-14	0.03	0.03	1.21	1.38	-0.09	0.12	0.04	0.06	-1.49	-1.31	-1.09
60649.162	-	-	2.740e-14	0.02	0.02	0.03	0.03	0.00	0.28	0.00	0.00	-	-	-0.89
60651.081	-	-	2.600e-14	0.02	0.03	0.00	0.00	0.00	0.25	0.00	0.00	-	-	-0.91
60671.078	-	-	2.050e-14	0.02	0.03	0.63	0.60	0.10	-0.07	0.03	0.02	-	-	-1.03
60673.083	1.370e-14	1.800e-14	3.17e-14	0.02	0.03	0.13	0.11	0.34	-0.02	0.01	0.00	-1.22	-1.09	-0.85
60678.091	8.500e-15	2.070e-14	2.92e-14	0.02	0.03	0.13	0.13	0.06	-0.05	0.01	0.00	-1.45	-1.02	-0.88

Notes. Dashed values stand for the epochs where we have blended emission. Therefore, we derive single integrated flux and $\log(L_{acc}/L_\odot)$ values added to the F_{total} and $\log(L_{acc,\text{total}}/L_\odot)$ columns.